

# Ab initio calculation of muon capture on $^{24}\text{Mg}$

L. Jokiniemi,<sup>1</sup> T. Miyagi,<sup>2,3</sup> S. R. Stroberg,<sup>4</sup> J. D. Holt,<sup>2,5</sup> J. Kotila,<sup>6,7,8</sup> and J. Suhonen<sup>8</sup>

<sup>1</sup>*Department of Quantum Physics and Astrophysics and Institute of Cosmos Sciences,  
University of Barcelona, 08028 Barcelona, Spain*

<sup>2</sup>*TRIUMF, 4004 Wesbrook Mall, Vancouver, BC V6T 2A3, Canada*

<sup>3</sup>*Technische Universität Darmstadt, Department of Physics, 64289 Darmstadt, Germany*

<sup>4</sup>*Department of Physics, University of Washington, Seattle, WA 98195, USA*

<sup>5</sup>*Department of Physics, McGill University, Montréal, QC H3A 2T8, Canada*

<sup>6</sup>*Finnish Institute for Educational Research, University of Jyväskylä, P.O. Box 35, Jyväskylä FI-40014, Finland*

<sup>7</sup>*Center for Theoretical Physics, Sloane Physics Laboratory,  
Yale University, New Haven, Connecticut 06520-8120, USA*

<sup>8</sup>*Department of Physics, University of Jyväskylä, P.O. Box 35, Jyväskylä FI-40014, Finland*

(Dated: November 29, 2021)

In this work we study ordinary muon capture on  $^{24}\text{Mg}$  from a first principles perspective. Starting from a particular two- and three-nucleon interaction derived from chiral effective field theory, we use the valence-space in-medium similarity renormalization group framework to construct effective Hamiltonians and muon capture operators which nonperturbatively account for many-body physics outside the valence space. The obtained nuclear matrix elements are compared against those from the phenomenological shell model. The impact of including the correlations from the nuclear shell model as well as including the induced two-body part is studied in detail. Furthermore, the effect of realistic bound-muon wave function on the operators is studied. Finally, predictions for capture rates to the lowest excited states in  $^{24}\text{Na}$  are given and compared with available data.

## I. INTRODUCTION

Ordinary muon capture (OMC) on nuclei is a nuclear-weak process, in which a negative muon  $\mu^-$  is captured by a nucleus  $(A, Z)$ , resulting in atomic number reduction by one, accompanied by emission of a muon neutrino. It can significantly extend the kinematic region of ordinary beta decay, owing to the high energy release and large momentum transfer involved in the process. The energy release in this process is on the order of 100 MeV, where the dominant fraction is carried by the neutrino. The large mass of the captured muon facilitates highly forbidden transitions and high excitation energies of the final states. These features make muon capture a particularly promising probe for the hypothetical neutrinoless double-beta ( $0\nu\beta\beta$ ) decay [1, 2].

Both the  $0\nu\beta\beta$  decay and OMC processes involve the axial-vector and pseudoscalar coupling constants  $g_A$  and  $g_P$ . In particular, the half-life of  $0\nu\beta\beta$  decay is inversely proportional to  $g_A^4$ . However, for decades many theoretical predictions for  $\beta$  decays have concluded that one must "quench" the  $g_A$  coupling in order to reproduce the measured half-lives [3]. While the  $g_A$  quenching puzzle related to  $\beta$  decays was recently solved from first principles in terms of neglected many-body correlations and two-body currents [4], the possible need for quenching at high-momentum exchange  $q \approx 100$  MeV is much less known. Since OMC operates at this same momentum-exchange regime, comparing theoretical predictions against measured OMC rates could shed light on this open question. Furthermore, while the free proton's pseudoscalar coupling is known to 1% [5], the correlation effects of  $g_P$  and corrections to the impulse approximation are under debate. In OMC calculations based

on the nuclear shell model [6–8], it has been seen that the Goldberger-Treiman partially conserved axial-vector-current hypothesis  $g_P/g_A = 6.8$  is not sufficient to reproduce experimental data. On the other hand, while the predictions for  $g_P$  based on chiral perturbation theory [9–11] agree with the value deduced from OMC (within large errors), they disagree with the one required by radiative muon-capture (RMC) experiments. Hence, OMC serves as an important probe of both these couplings.

The relevance of OMC to  $0\nu\beta\beta$  decay is of interest to both experimentalists and theorists [12]. There are several theoretical predictions for the OMC rates and the involved matrix elements based on the nuclear shell model (NSM) [1, 2, 6–8, 13, 14], and proton-neutron quasi-particle random-phase approximation (pnQRPA) [15–18] frameworks. More recently, there are also ab initio calculations for the muon-capture rates in very light,  $A \leq 6$ , nuclei based on quantum Monte Carlo methods [19, 20]. A recent pnQRPA-based study on the OMC strength function in  $^{100}\text{Nb}$  [21] showed good agreement with the experimental counterpart measured at RCNP, Osaka [22]. Also partial OMC rates to the excited states of intermediate nuclei of several  $\beta\beta$ -decay triplets have already been measured [23], and these studies are planned to be extended to the remaining  $\beta\beta$ -decay cases.

In particular, OMC on  $^{24}\text{Mg}$  is interesting for many reasons. First, the  $sd$ -shell nuclei  $^{24}\text{Mg}$  and  $^{24}\text{Na}$  are relatively well studied both experimentally and theoretically and accessible to ab initio methods [24, 25]. In addition, the conveniently long lifetime (1067 ns) of the muonic  $^{24}\text{Mg}$  atom [26], the well-isolated low-lying  $1^+$  states in the final nucleus,  $^{24}\text{Na}$ , and the naturally high abundance of  $^{24}\text{Mg}$  (79 %) all make it an appealing experimental candidate. Partial OMC rates to low-lying

states in  $^{24}\text{Na}$  have been measured at TRIUMF [27], and more recently preliminary measurements aiming to expand the study of OMC on  $^{24}\text{Mg}$  have been performed at PSI, Switzerland [28]. In this work we study OMC on  $^{24}\text{Mg}$  from an ab initio perspective, utilizing realistic bound-muon wave functions, for the first time. In particular, we use the valence-space in-medium similarity renormalization group (VS-IMSRG) [29–31] to consistently transform Hamiltonians and muon capture operators. We compare the obtained nuclear matrix elements against the results computed in the nuclear shell-model framework with the USDB interaction. Finally, we compare the resulting capture rates with available experimental data [27]. The present work serves a first-step benchmark towards calculating capture rates relevant for all future measurements.

## II. MUON-CAPTURE FORMALISM

OMC is a semileptonic weak-interaction process similar to electron capture (EC). Here we are interested in OMC on the ground state of  $^{24}\text{Mg}$ :

$$\mu^- + {}^{24}\text{Mg}(0_{\text{g.s.}}^+) \rightarrow \nu_\mu + {}^{24}\text{Na}(J^\pi), \quad (1)$$

where a negative muon ( $\mu^-$ ) is captured by the  $0^+$  ground state of the even-even nucleus  $^{24}\text{Mg}$  with atomic number  $Z = 12$ . The process leads to the  $J^\pi$  multipole states of  $^{24}\text{Na}$ , the odd-odd isobar of the mother nucleus, of atomic number  $Z = 11$ ; here  $J$  is the angular momentum and  $\pi$  the parity of the final state. At the same time a muon neutrino  $\nu_\mu$  is emitted. The forbiddenness ( $n$ ) of a muon-capture transition can be defined in the same way as for  $\beta$  decay (see Table I).

### A. Bound-Muon Wave Functions

The wave function of a muon bound in an atomic orbit of the mother nucleus can be expressed as an expansion in terms of the normalized spherical spinors  $\chi_{\kappa\mu}$

$$\psi_\mu(\kappa, \mu; \mathbf{r}) = \psi_{\kappa\mu}^{(\mu)} = \begin{bmatrix} -iF_\kappa \chi_{-\kappa\mu} \\ G_\kappa \chi_{\kappa\mu} \end{bmatrix}, \quad (2)$$

where  $G_\kappa$  and  $F_\kappa$  are the radial wave functions of the bound state [32]. Here  $\kappa$  denotes the atomic orbit in the following manner

$$\begin{cases} l = \kappa \text{ and } j = l - \frac{1}{2}, & \text{for } \kappa > 0 \\ l = -\kappa - 1 \text{ and } j = l + \frac{1}{2}, & \text{for } \kappa < 0. \end{cases} \quad (3)$$

After being stopped in the outer shells of an atom, the negative muon goes through a series of transitions to lower atomic orbitals, leaving it finally on the lowest,  $K$  atomic orbit. Hence, the captured muon can be assumed to be initially bound in the lowest state  $1s_{1/2}$ , corresponding

TABLE I. Forbiddenness rules for ordinary muon capture.

$n$	Spin change $ J_f - J_i $	Parity change $\pi_f \pi_i$
0	0,1	+1
1	0,1,2	-1
$\geq 2$	$n, n+1$	$(-1)^n$

to  $\kappa = -1$  and  $\mu = \pm \frac{1}{2}$ . Treating the mother nucleus as a point-like particle, we can approximate the wave function of the  $1s_{1/2}$  atomic orbit by the Bethe-Salpeter (BS) approximation formula [33]. Taking  $\hbar = c = 1$  we then have

$$G_{-1} = (2Z/a_0)^{\frac{3}{2}} \sqrt{\frac{1+\gamma}{2\Gamma(2\gamma+1)}} \left(\frac{2Zr}{a_0}\right)^{\gamma-1} e^{-Zr/a_0},$$

$$F_{-1} = -\sqrt{\frac{1-\gamma}{1+\gamma}} G_{-1}. \quad (4)$$

Here  $\alpha$  is the fine structure constant,  $Z$  the atomic number of the nucleus,  $\gamma = \sqrt{1 - (\alpha Z)^2}$ , and

$$a_0 = \frac{1}{m'_\mu \alpha}$$

is the Bohr radius of the  $\mu$ -mesonic atom. Here we have defined the reduced muon mass as

$$m'_\mu = \frac{m_\mu}{1 + \frac{m_\mu}{AM}} \quad (5)$$

where  $M$  is the (average) nucleon mass, and  $AM$  is the mass of the mother (and daughter) nucleus. For a light nucleus, as in the present case,  $\alpha Z$  is small and we can approximate  $\gamma \approx 1$ , leading to

$$G_{-1} = 2(\alpha Z m'_\mu)^{\frac{3}{2}} e^{-\alpha Z m'_\mu r}, \quad (6)$$

$$F_{-1} = 0.$$

The approximation is similar to the hydrogen-like Schrödinger equation with a modified  $a_0$ . This is the adopted form for the bound-muon wave function in Ref. [32], and also our starting point in the present study.

In order to take the finite size of the nucleus properly into account, we construct a realistic bound-muon wave function by solving the Dirac wave equations [34] for the large,  $G_{-1}$ , and small,  $F_{-1}$ , parts of the wave function (2) in the Coulomb field created by the nucleus. Assuming the muon is bound in the lowest state  $1s_{1/2}$  ( $\kappa = -1$ ), the components satisfy the coupled differential equations

$$\begin{cases} \frac{d}{dr} G_{-1} + \frac{1}{r} G_{-1} = \frac{1}{\hbar c} (mc^2 - E + V(r)) F_{-1}, \\ \frac{d}{dr} F_{-1} - \frac{1}{r} F_{-1} = \frac{1}{\hbar c} (mc^2 + E - V(r)) G_{-1}. \end{cases} \quad (7)$$

Taking a uniform distribution of the nuclear charge within the charge radius  $R_c = r_0 A^{1/3}$ , the potential energy  $V(r)$  in Eqs. (7) can be written:

$$V(r) = \begin{cases} -\frac{Ze^2}{2R_c} \left[ 3 - \left(\frac{r}{R_c}\right)^2 \right], & \text{if } r \leq R_c \\ -\frac{Ze^2}{r}, & \text{if } r > R_c. \end{cases} \quad (8)$$

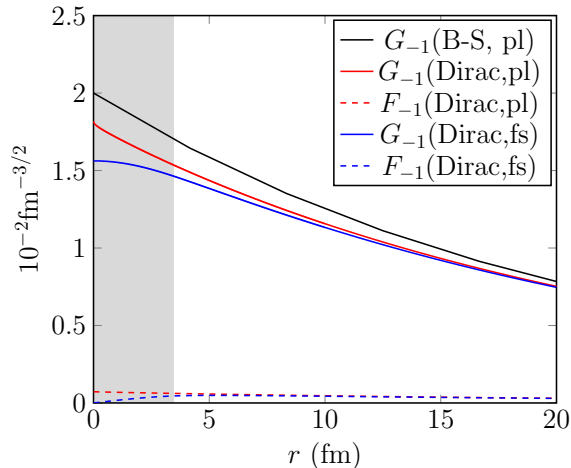


FIG. 1. Large ( $G_{-1}$ ) and small ( $F_{-1}$ ) components of the bound-muon wave functions in  $^{24}\text{Mg}$ . 'B-S' refers to the BS approximation and 'Dirac' to the exact wave function from the Dirac equation. 'pl' and 'fs' refer to point-like nucleus and finite-size nucleus. The shaded area corresponds to the interior of the  $^{24}\text{Mg}$  nucleus.

These equations (7) can then be solved by means of the package RADIAL [35] using a piece-wise-exact power-series expansion of the radial functions, which are summed to the prescribed accuracy. A similar method has previously been used for bound-electron wave functions in the context of  $\beta\beta$  decay [36, 37].

In Fig. 1 we plot the amplitudes  $G_{-1}$  and  $F_{-1}$  as solved from the Dirac equations (solid and dashed blue lines, correspondingly) and contrast them with those obtained from the BS approximation (black line) of Eq. (6). The small part vanishes in the BS approximation and thus does not appear in the figure. For comparison, we have also plotted the exact solution of the Dirac equation corresponding to point-like nucleus (solid and dashed red lines). The behavior of the Dirac wave function corresponding to the point-like nucleus is essentially similar to the BS approximation, even though the values at  $r \approx 0$  are slightly different. When the finite size of the nucleus is taken into account, the Dirac wave function is notably suppressed at  $r \lesssim 5$  fm, i.e. inside the nucleus. As illustrated in the figure, the small part of the exact solution is negligible compared to the large part, hence we can safely neglect it in the calculations. This is expected, since the small part is suppressed by  $v/c = Z\alpha$ .

## B. Muon-Capture Matrix Elements

We compute the OMC matrix elements using the formalism originally developed by Morita and Fujii in [32]. The formalism takes into account both the genuine and induced vector and axial-vector weak nucleon currents. The formalism is rather involved, and here we only

present the main ingredients needed in the calculations. Further details on the derivations of the equations can be found in [32, 38]. Here it is appropriate to note that in Ref. [39] it was found that momentum-dependent two-body hadronic currents could have an impact on the  $0\nu\beta\beta$ -decay nuclear matrix elements (NMEs). Owing to the similar momentum-exchange scales, the effects of two-body currents could be expected to be similar for OMC. The currents have already been included in OMC calculations of light nuclei [19, 20], but the effects in heavier nuclei have yet to be explored. Nonetheless, the two-body currents (see the derivation in [40]) together with appropriate low-energy constants [41–44] should be included in the formalism.

The matrix elements for a transition from an initial  $J_i$  state to a final  $J_f$  state can be defined as

$$\begin{aligned} & \int \Psi_{J_f M_f} \sum_{s=1}^A \mathcal{O}_s \tau_s^\pm \Psi_{J_i M_i} d\mathbf{r}_1 \dots d\mathbf{r}_A \\ & = \mathcal{M}[k w u \begin{pmatrix} \pm \\ p \end{pmatrix}](J_i M_i u M_f - M_i | J_f M_f), \end{aligned} \quad (9)$$

where  $\Psi_{J_i M_i}$  and  $\Psi_{J_f M_f}$  are the nuclear wave functions corresponding to the initial and final state. The operators  $\mathcal{O}_s$  in (9) are defined in Table II. Here we assume that the muon is bound on the  $\kappa = -1$  orbit and that the small component of the bound-muon wave function is negligible as clearly demonstrated in Fig. 1. The small component is only about 0.1% of the large component at  $r < R_c$ . Neglecting the small component simplifies the expressions of the matrix elements considerably (see Table I of Ref. [32]).

In Table II,  $j_w(qr_s)$  is the spherical Bessel function of rank  $w$ . The quantities  $\mathcal{Y}_{k w u}^M$  are the (vector) spherical harmonics defined as

$$\begin{aligned} \mathcal{Y}_{0 w u}^M(\hat{\mathbf{r}}) & \equiv (4\pi)^{-1/2} Y_{w, M}(\hat{\mathbf{r}}), \\ \mathcal{Y}_{1 w u}^M(\hat{\mathbf{r}}, \boldsymbol{\sigma}) & \equiv \sum_m (1 - m w m + M | u M) \\ & \quad \times Y_{w, m+M}(\hat{\mathbf{r}}) \sqrt{\frac{3}{4\pi}} \sigma_{-m}, \\ \mathcal{Y}_{1 w u}^M(\hat{\mathbf{r}}, \mathbf{p}) & \equiv \sum_m (1 - m w m + M | u M) \\ & \quad \times Y_{w, m+M}(\hat{\mathbf{r}}) \sqrt{\frac{3}{4\pi}} p_{-m}, \end{aligned} \quad (10)$$

where  $\boldsymbol{\sigma}$  is the Pauli spin vector,  $\mathbf{p}$  is the nucleon momentum,  $Y_{w, M}(\hat{\mathbf{r}})$  are the spherical harmonics, and  $\hat{\mathbf{r}}$  is the unit coordinate vector for angles in spherical coordinates.

The  $q$  in Table II is the  $Q$ -value of the capture process:

$$q = (m_\mu - W_0) \left( 1 - \frac{m_\mu}{2(m_\mu + AM)} \right), \quad (11)$$

where  $W_0 = M_f - M_i + m_e + E_X$ . Here  $M_f(M_i)$  is the nuclear mass of the final(initial) nucleus,  $m_e$  the rest mass of an electron,  $m_\mu$  the rest mass of a muon,  $M$  the

TABLE II. Definition of  $\mathcal{O}_s$  in Eq. (9) for different OMC nuclear matrix elements (NMEs).

NME	$\mathcal{O}_s$
$\mathcal{M}[0 w u]$	$j_w(qr_s)G_{-1}(r_s)\mathcal{Y}_{0wu}^{M_f-M_i}(\hat{\mathbf{r}}_s)\delta_{wu}$
$\mathcal{M}[1 w u]$	$j_w(qr_s)G_{-1}(r_s)\mathcal{Y}_{1wu}^{M_f-M_i}(\hat{\mathbf{r}}_s, \boldsymbol{\sigma}_s)$
$\mathcal{M}[0 w u \pm]$	$[j_w(qr_s)G_{-1}(r_s) \mp \frac{1}{q}j_{w\mp 1}(qr_s)\frac{d}{dr_s}G_{-1}(r_s)]\mathcal{Y}_{0wu}^{M_f-M_i}(\hat{\mathbf{r}}_s)\delta_{wu}$
$\mathcal{M}[1 w u \pm]$	$[j_w(qr_s)G_{-1}(r_s) \mp \frac{1}{q}j_{w\mp 1}(qr_s)\frac{d}{dr_s}G_{-1}(r_s)]\mathcal{Y}_{1wu}^{M_f-M_i}(\hat{\mathbf{r}}_s, \boldsymbol{\sigma}_s)$
$\mathcal{M}[0 w u p]$	$ij_w(qr_s)G_{-1}(r_s)\mathcal{Y}_{0wu}^{M_f-M_i}(\hat{\mathbf{r}}_s)\boldsymbol{\sigma}_s \cdot \mathbf{p}_s\delta_{wu}$
$\mathcal{M}[1 w u p]$	$ij_w(qr_s)G_{-1}(r_s)\mathcal{Y}_{1wu}^{M_f-M_i}(\hat{\mathbf{r}}_s, \mathbf{p}_s)$

average nucleon mass, and  $E_X$  the excitation energy of the final  $J^\pi$  state. At low excitation energies,  $W_0/m_\mu \ll 1$ , so the operators do not significantly depend on the excitation energy.

In NSM calculations, the matrix elements of Eq. (9) are expressed in terms of reduced matrix elements:

$$\mathcal{M}_\mu = \hat{J}_f^{-1} \sum_{pn} \mathcal{O}_{\mu,np} T_{J_f J_i, np}^u, \quad (12)$$

where indices  $p$  and  $n$  label proton and neutron orbitals, respectively. Here  $T_{J_f J_i, np}^u$  is the one-body transition density (OBTD)

$$\begin{aligned} T_{J_f J_i, np}^u &= \frac{1}{\hat{u}} \langle J_f || [c_n^\dagger \tilde{c}_p]_u || J_i \rangle, \\ \tilde{c}_p &= (-1)^{j_p - m_p} c_p \end{aligned} \quad (13)$$

and we adopt the shorthand notation  $\mu = [k w u (\pm)_p]$  for one-body transition matrix elements  $\mathcal{O}_{\mu,np}$ , corresponding to the operators given in Table II. We evaluate these matrix elements in the harmonic oscillator (HO) basis.

### C. Capture Rates

The capture rate for a transition from a  $J_i^\pi$  initial state to a  $J_f^\pi$  final state can be written as

$$W = 2P \frac{2J_f + 1}{2J_i + 1} \left( 1 - \frac{q}{m_\mu + AM} \right) q^2, \quad (14)$$

with

$$P = \frac{1}{2} \sum_{\kappa u} \left| A + B + C + D + E + F + G \right|^2, \quad (15)$$

where the quantities  $A$ - $G$  depend on  $\kappa$  and  $u$  and are defined as

$$A = g_V \mathcal{M}[0 l u] S_{0u}(\kappa) \delta_{lu}, \quad (16)$$

$$B = g_A \mathcal{M}[1 l u] S_{1u}(\kappa), \quad (17)$$

$$C = -\frac{g_V}{M} \mathcal{M}[1 \bar{l} u p] S'_{1u}(-\kappa), \quad (18)$$

$$\begin{aligned} D &= \sqrt{3} \frac{g_V q}{2M} \left( \sqrt{\frac{\bar{l}+1}{2\bar{l}+3}} \mathcal{M}[0 \bar{l}+1 u+] \delta_{\bar{l}+1,u} \right. \\ &\quad \left. + \sqrt{\frac{\bar{l}}{2\bar{l}-1}} \mathcal{M}[0 \bar{l}-1 u-] \delta_{\bar{l}-1,u} \right) S'_{1u}(-\kappa), \end{aligned} \quad (19)$$

$$\begin{aligned} E &= \sqrt{\frac{3}{2}} \left( \frac{g_V q}{M} \right) (1 + \mu_p - \mu_n) S'_{1u}(-\kappa) \\ &\quad \times \left( \sqrt{\bar{l}+1} W(1 1 u \bar{l}; 1 \bar{l}+1) \mathcal{M}[1 \bar{l}+1 u+] \right. \\ &\quad \left. + \sqrt{\bar{l}} W(1 1 u \bar{l}; 1 \bar{l}-1) \mathcal{M}[1 \bar{l}-1 u-] \right), \end{aligned} \quad (20)$$

$$F = -\left( \frac{g_A}{M} \right) \mathcal{M}[0 \bar{l} u p] S'_{0u}(-\kappa) \delta_{\bar{l}u}, \quad (21)$$

and

$$\begin{aligned} G &= \sqrt{\frac{1}{3}} \frac{q}{2M} (g_P - g_A) S'_{0u}(-\kappa) \delta_{\bar{l}u} \\ &\quad \times \left( \sqrt{\frac{\bar{l}+1}{2\bar{l}+1}} \mathcal{M}[1 \bar{l}+1 u+] + \sqrt{\frac{\bar{l}}{2\bar{l}+1}} \mathcal{M}[1 \bar{l}-1 u-] \right). \end{aligned} \quad (22)$$

The  $W(\dots)$  in Eqs. (16-22) are the usual Racah coefficients and the  $S$ 's are geometric factors defined as

$$S_{ku}(\kappa) = \begin{cases} \sqrt{2(2j+1)} W(\frac{1}{2} 1 j l; \frac{1}{2} u) \delta_{lu}, & \text{for } k = 1 \\ \sqrt{\frac{2j+1}{2l+1}} \delta_{lu}, & \text{for } k = 0 \end{cases} \quad (23)$$

and

$$S'_{ku}(-\kappa) = \text{sgn}(\kappa) S_{ku}(-\kappa), \quad (24)$$

where  $\text{sgn}(\kappa)$  is the sign of  $\kappa$ . The angular momenta  $l$  and  $\bar{l}$  correspond to  $\kappa$  and  $-\kappa$  respectively. We use the Goldberger-Treiman partially conserved axial-vector-current (PCAC) value  $g_P/g_A = 6.8$  for the ratio of the pseudoscalar and axial-vector coupling strengths. For the axial-vector coupling we use the free-nucleon value  $g_A = 1.27$ . The explicit expressions for the  $P$  of Eq. (15) containing all the next-to-leading order terms can be found e.g. in Ref. [38]. Note that in Ref. [32] the terms of the order  $1/M^2$  were omitted from the explicit expressions for  $P$ .

### III. MANY-BODY METHODS

#### A. Valence-space in-medium similarity renormalization group

In this work we use the ab initio VS-IMSRG [31, 45–47], to construct a continuous ( $s$ -dependent) unitary transformation  $U(s)$ , to decouple an effective valence-space Hamiltonian  $U(s)HU^\dagger(s)$  from the full Hilbert space. In the VS-IMSRG, based on the exponential ansatz  $U(s) = e^{\Omega(s)}$  with the anti-Hermitian operator  $\Omega(s)$ , one finds  $\Omega(s)$  by solving the flow equation [48]:

$$\frac{d\Omega}{ds} = \sum_{n=1}^{\infty} \frac{B_n}{n!} \text{ad}_\Omega^n(\eta), \quad \text{ad}_\Omega^n = [\Omega, \text{ad}_\Omega^{n-1}], \quad (25)$$

with  $\text{ad}_\Omega^0 = \eta$  and  $\Omega(0) = 0$ . The object  $\eta$  is known as the generator of the flow equation, and we use the arctangent generator in this work. With the same unitary transformation, any valence-space effective operator can be derived consistently [49].

The actual calculation procedure is as follows. We begin from a nuclear Hamiltonian based on chiral effective field theory [50, 51] expressed in the 13 major-shell HO space at the frequency 16 MeV. In the current study, the employed interaction is the two (NN) and three-nucleon (3N) force 1.8/2.0 (EM) [52, 53], where the NN force is given at order N<sup>3</sup>LO and the 3N force at N<sup>2</sup>LO. This interaction has been shown to reproduce ground-state energies globally to the <sup>132</sup>Sn region and beyond [54–56], while generally giving too small radii [57]. For the 3N piece, due to memory limitations, we need to introduce an additional truncation  $E_{3\text{max}} = 24$  [56] defined as the sum of the three-body HO quanta. Before solving the flow equation (25), we optimize the single-particle orbitals through transformation to the Hartree-Fock (HF) basis. Since the evolution of the full 3N Hamiltonian in a realistic model space is challenging [58], we employ the ensemble normal-ordering [30] technique to capture 3N forces between valence nucleons.

During the VS-IMSRG evolution, all the operators are truncated at the two-body level, referred to as the VS-IMSRG(2) approximation. As a consequence, the originally one-body OMC operators have both one- and in-

duced two-body terms:

$$\bar{O}_\mu = e^{\Omega(s)} O_\mu e^{-\Omega(s)} \approx \bar{O}_\mu^{(1)} + \bar{O}_\mu^{(2)}$$

Combining the consistently evolved operators and the one- and two-body transition density matrices, we compute the NMEs:

$$\hat{J}_f \mathcal{M}_\mu \approx \sum_{pq} \bar{O}_{\mu,pq}^{(1)} T_{J_f J_i, pq}^u + \frac{1}{4} \sum_{pqrs} \sum_{J_{pq} J_{rs}} \bar{O}_{\mu,pqrs}^{(2)J_{pq} J_{rs}} T_{J_f J_i, pqrs}^{J_{pq} J_{rs} u}, \quad (26)$$

with the evolved OMC operator matrix elements  $\bar{O}_{\mu,pq}^{(1)}$  and  $\bar{O}_{\mu,pqrs}^{(2)J_{pq} J_{rs}}$ , and  $p, q, r$  and  $s$  running through all possible proton and neutron states. In addition to the OBTD  $T_{J_f J_i, pq}^u$ , the two-body transition density  $T_{J_f J_i, pqrs}^{J_{pq} J_{rs} u}$  is introduced as

$$\begin{aligned} T_{J_f J_i, pqrs}^{J_{pq} J_{rs} u} &= \frac{1}{\tilde{u}} \langle J_f || [A_{pq, J_{pq}}^\dagger \tilde{A}_{rs, J_{rs}}] u || J_i \rangle, \\ A_{pq, J_{pq} M_{pq}}^\dagger &= \frac{1}{\sqrt{1 + \delta_{pq}}} [c_p^\dagger c_q^\dagger]_{J_{pq} M_{pq}}, \\ \tilde{A}_{pq, J_{pq} M_{pq}} &= \frac{1}{\sqrt{1 + \delta_{pq}}} [\tilde{c}_p \tilde{c}_q]_{J_{pq} - M_{pq}}. \end{aligned} \quad (27)$$

Note that  $\delta_{pq}$  indicates  $\delta_{n_p n_q} \delta_{l_p l_q} \delta_{j_p j_q} \delta_{t_z, p t_z, q}$  with the nodal quantum number, orbital angular momentum, total angular momentum, and label distinguishing proton and neutron, respectively. The flow equations are solved with `imsrg++` code [59], and the valence-space diagonalization and computation of the corresponding transition densities are performed with the `KSHELL` code [60].

#### B. Nuclear Shell Model

We also compare the VS-IMSRG results with those of phenomenological NSM calculations performed using the NuShellX@MSU code [61] in the  $sd$ -shell with the USDB interaction [62]. The interaction is based on a renormalized  $G$ -matrix with two-body matrix elements adjusted to experimental binding and excitation energies of  $sd$ -shell nuclei. Hence, the interaction reproduces the spectroscopic properties of  $sd$ -shell nuclei well. As NSM is a phenomenological method, the fitted Hamiltonian and bare OMC operator are inconsistent. For the NSM calculations, we use a HO basis with frequency obtained from the Blomqvist-Molinari formula [63]  $\hbar\omega = (45A^{-1/3} - 25A^{-2/3})$  MeV for evaluating the operator matrix elements. However, the single-particle basis is based on the USDB interaction and thereby differs from the HO basis. Furthermore, in the NSM we are restricted to the  $sd$ -shell, and contributions to OMC from outside the valence space are not accounted for with the bare transition operator.



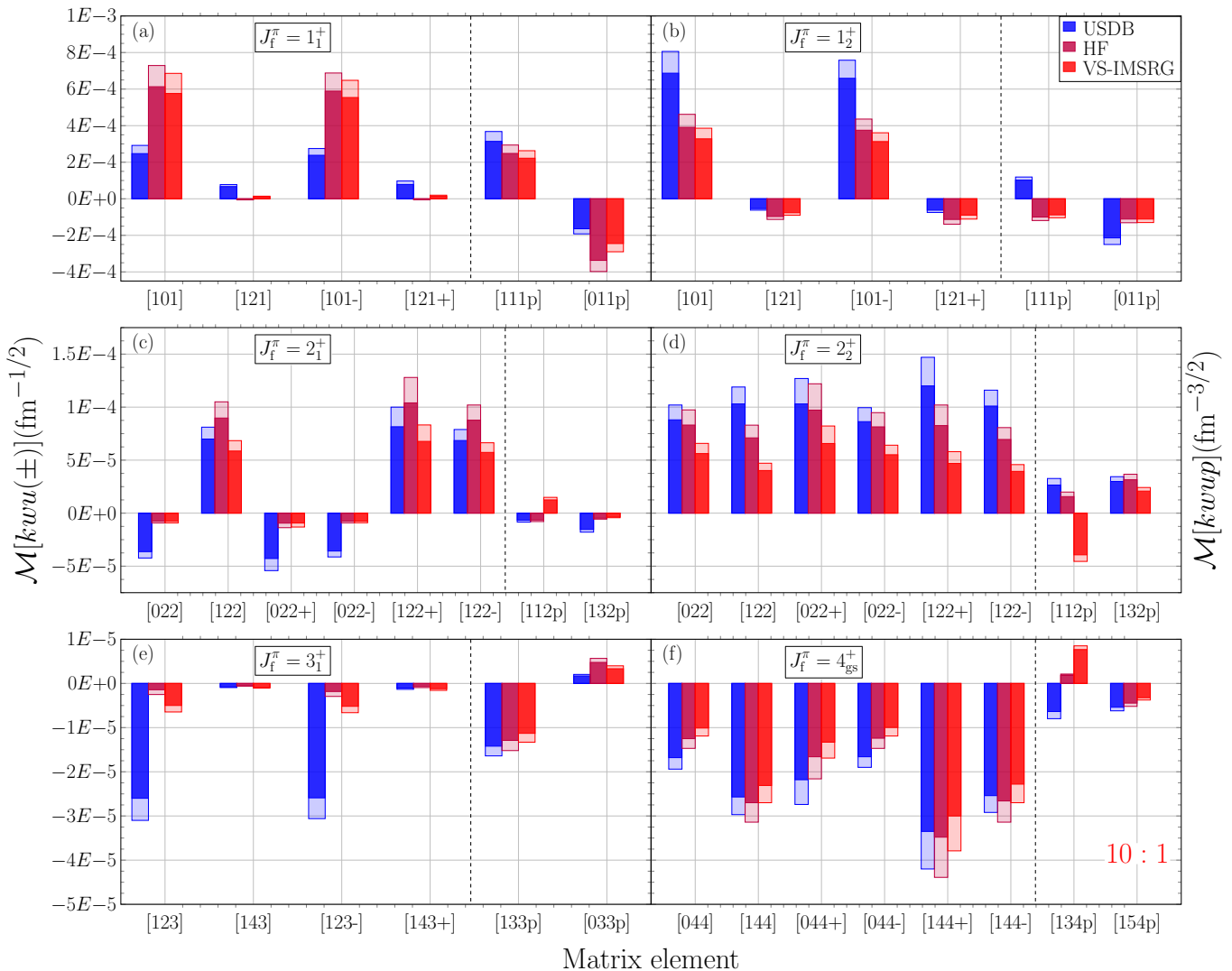


FIG. 2. Nuclear matrix elements for the transitions  $\mu^- + {}^{24}\text{Mg}(0_{\text{g.s.}}^+) \rightarrow \nu_\mu + {}^{24}\text{Na}(J_f^\pi)$  to a few lowest  $J^\pi$  states in  ${}^{24}\text{Na}$ . The dark bars are computed with the Dirac wave functions and the light bars with the BS approximation. Thus, the difference shows the finite-size effect. The matrix elements of the type  $\mathcal{M}[kwp]$  – separated by the vertical dashed line – are given in  $\text{fm}^{-3/2}$ , while the rest are in units  $\text{fm}^{-1/2}$ . The NMEs in panel (f) are multiplied by 10.

## IV. RESULTS AND DISCUSSION

### A. Nuclear Matrix Elements

In Fig. 2 we show the computed OMC NMEs for the transitions to the lowest states in  ${}^{24}\text{Na}$ . We compare the NMEs computed in the VS-IMSIRG framework with those obtained in the NSM with the USDB interaction and OMC operators expressed in the HO basis. The  $q$ -values in the operators correspond to the experimental excitation energies. The ‘HF’ in the figures refers to the matrix elements calculated with the decoupled VS-IMSIRG Hamiltonian and the operators evaluated in the Hartree-Fock basis (i.e. without consistent IMSRG evolution). Hence, the HF results do not contain the two-body induced terms in the VS-IMSIRG procedure. The dark bars

for each framework are computed with the bound-muon wave function solved from the Dirac equation taking into account the finite size of the nucleus, whereas the light bars are computed with the BS point-like approximation introduced in Sec. II A. Hence, the difference shows the effect coming from finite-size nucleus. Note that the momentum-dependent matrix elements of the type  $\mathcal{M}[kwp]$  are given in units  $\text{fm}^{-3/2}$  here, while the rest are given in units  $\text{fm}^{-1/2}$ .

The finite-size effect is rather consistent for all NMEs: taking this into account decreases the absolute value by 15 – 20%. The finite-size effect is slightly larger in the NMEs of the type  $[kwp+]$ , whereas the effect is somewhat less visible for  $[kwp-]$ . These small differences can be explained by the derivative terms in  $[kwp\pm]$  (see Table II) that are not present in the other matrix elements.

TABLE III. Ordinary muon capture rates to the low-lying states in  $^{24}\text{Na}$  computed in the NSM and VS-IMSRG frameworks. The capture rates are computed with the Dirac (fs) bound-muon wave function (with the BS approximation).

$J_i^\pi$	$E$ (MeV)			Rate (1/s)	
	Exp.	NSM	IMSRG	NSM	IMSRG
$4_{\text{g.s.}}^+$	0.0	0.0	0.0	2.3 (3.1)	1.6 (2.3)
$1_1^+$	0.472	0.540	0.397	3 278.5 (4 527)	18 077 (25 524)
$2_1^+$	0.563	0.629	0.244	755.9 (1 024)	390 (535)
$2_2^+$	1.341	1.107	0.865	2 447.4 (3 356)	813 (1 126)
$3_1^+$	1.345	1.338	0.915	87.0 (123.0)	3.9 (6.3)
$1_2^+$	1.347	1.324	0.821	26 435.8 (36 013)	6 235 (8 606)

Note that the finite-size effect on the matrix elements is similar to that on the wave function at  $r = 0$  in Fig. 1.

The ‘HF’ bars can be considered an intermediate step between the ‘USDB’ and ‘VS-IMSRG’ results. In most cases the ‘HF’ NMEs are closer to ‘VS-IMSRG’ than ‘USDB’. This means that in most cases, transforming the OMC operators and including the two-body terms have a relatively small effect on the NMEs. However, particularly for transitions to  $2_{1,2}^+$  states, including the two-body term has a strong effect on the  $[112p]$  NME: including the two-body term in ‘VS-IMSRG’ changes the sign (see panels (c) and (d) in Fig. 2). In order to further study the effects coming from the IMSRG transformation and the induced two-body part, we compare the ‘USDB’ NMEs against the one- and two-body parts and the total IMSRG matrix elements in Fig. 3 in the Appendix. These figures confirm the perceptions mentioned above: the IMSRG two-body term indeed is sizeable but of the opposite sign especially in the case of the  $[112p]$  NME, as can be seen in panels (c) and (d) of Fig. 3. In addition, for the transition to  $4_{\text{g.s.}}^+$ , shown in panel (f) of Fig. 3, we see that the two-body term increases the value of the  $[134p]$  NME by  $\approx 50\%$ .

On the other hand, we note that using the VS-IMSRG wave functions instead of those of the NSM has a strong effect on the NMEs. This can be seen if we compare the ‘USDB’ bars with the ‘HF’ or ‘VS-IMSRG’. This stems from the fact that in the VS-IMSRG calculations, the operators and excitations are derived consistently with the same unitary transformation, while in the NSM calculations, the excitations outside the valence space are implicitly accounted for by the effective interaction but the operator is not adjusted correspondingly. In order to distinguish effects coming from the different wave functions versus transforming the operator, we show the one-body parts of the NMEs obtained with different OBTD/operator combinations: we use either the USDB or the IMSRG OBTDs together with either the HO operator or the IMSRG-transformed operator. The results are given in Tables V-X in the Appendix. In most cases, the transformed operator does not significantly change the NME, while the OBTD has a more pronounced effect: in many cases the NMEs obtained with different

OBTDs are opposite in sign. Interestingly, the effect of the VS-IMSRG on the matrix element  $[101]$  (and  $[101-]$ , which differs from  $[101]$  only by the small derivative term) is the opposite for the states  $1_1^+$  and  $1_2^+$ : where the VS-IMSRG result is larger than the USDB one for the first  $1^+$  state, the situation is the opposite for the second  $1^+$  state. This is likely due to mixing of these two states.

## B. Capture Rates

Finally, in Table III we give capture rates to the lowest states in  $^{24}\text{Na}$  obtained from the calculated NMEs. We show the capture rates obtained with both the realistic bound-muon wave function as well as those with the BS pointlike-nucleus approximation. For each state we give the experimental and calculated excitation energies in addition to the corresponding capture rates obtained from the NSM and VS-IMSRG calculations. The capture rates obtained with the BS pointlike-nucleus approximation are shown in parentheses.

While excitation energies have a negligible direct impact on the capture rate through (11), excitation energies are often used as an indirect probe of the quality of shell-model wave functions. In Table III we see that the NSM better reproduces the experimental excitation energies than VS-IMSRG. This is expected, since the USDB interaction is tuned to reproduce the spectroscopic properties of  $sd$ -shell nuclei, whereas the 1.8/2.0 (EM) chiral Hamiltonian used in the VS-IMSRG is only fit to few-body data. Consequently, the possibility of overconstraining excitation energies (at the expense of observables like OMC, which are not included in the fit) means this proxy should not be given undue weight.

Comparing the obtained capture rates in columns 7-10 of Table III we see that the OMC rates for the VS-IMSRG and the NSM show an overall consistent pattern for all states except the  $1^+$  states which seem to be interchanged between the two calculations. The only notable difference in the magnitudes of the OMC rates, excluding the  $1^+$  states, concerns the OMC to the  $3_1^+$  state, with a factor of 20 difference.

Concerning the  $1^+$  states, the behavior of the matrix elements  $[101]$  and  $[101-]$  is reflected in the capture rates: VS-IMSRG predicts a notably larger rate to  $1_1^+$  and a smaller rate to  $1_2^+$  compared to the NSM. This is reasonable since the  $[101]$  and  $[101-]$  NMEs are dominant for these transitions. The finite-size effect of the NMEs is shown to be rather constant, reducing the capture rates by 30 – 40%, keeping with the finite-size effect of the NMEs. This is also consistent with the scaling factor  $(Z_{\text{eff}}/Z)^4 = (10.69/12)^4 \approx 0.63$  (for  $^{24}\text{Mg}$ ) [26] used in the previous studies to account for the finite-size effect.

Finally, we compare the computed capture rates to the  $1^+$  and  $2^+$  states with the partial muon capture rates reported in Ref. [27]. They measured the direct (produced by muon-capture on the ground state of  $^{24}\text{Mg}$ ) and indirect (produced by muon-capture on an excited state

TABLE IV. Comparison between the computed capture rates and the experimental partial muon capture rates obtained from Ref. [27] (see text) to the low-lying  $1^+$  and  $2^+$  states in  $^{24}\text{Na}$ . The uncertainties of the summed rates are obtained by summing up uncertainties of individual capture rates. The computed rates correspond to the rounded values of Table III.

$J_i^\pi$	$E_{\text{exp}}$ (MeV)	Rate ( $10^3$ 1/s)		
		Exp.[27]	NSM	IMSRG
$1_1^+$	0.472	$21.0 \pm 6.6^{\text{a}}$	3.3	18.1
$1_2^+$	1.347	$17.5 \pm 2.3$	26.4	6.2
Sum( $1^+$ )		$38.5 \pm 8.9$	29.7	24.3
$2_1^+$	0.563	$17.5 \pm 2.1$	0.8	0.4
$2_2^+$	1.341	$3.4 \pm 0.5$	2.4	0.8
Sum( $2^+$ )		$20.9 \pm 2.6$	3.2	1.2

<sup>a</sup> Unidentified cascade feeding of the state is suspected.

of  $^{24}\text{Mg}$ )  $\gamma$ -ray yields to a few low-lying states in  $^{24}\text{Na}$ . The partial muon-capture rates can be obtained by multiplying the direct state yields by the appropriate total muon-capture rates [26]. The obtained values, together with the capture rates obtained in the present work, are tabulated in Table IV. It should be noted, however, that obtaining the direct-state yields requires knowledge of cascade feeding, and only a small fraction of the  $\gamma$ -rays could be identified in Ref. [27]. Therefore all values could be slightly reduced following the discovery of more transitions. As for the  $1_1^+$  state, the authors suspected that the cascade feeding was unidentified.

We note that while the capture rates to the lowest two  $1^+$  states in Table IV seem to be interchanged in the NSM and VS-IMSRG, the summed rates to these two states agree within 20%. Clearly both of the estimates are notably smaller than the experimental counterpart, which could be explained by potentially unidentified  $\gamma$ -rays. For the  $2^+$  states the differences are more prominent: the NSM- and VS-IMSRG-calculated summed rates disagree almost by a factor of three, while the experimental value is an order of magnitude larger than the computed values. Most of the difference appears to be coming from the capture rates to the  $2_1^+$  state, where the theory predictions are  $\approx 20 - 40$  times smaller than the measured rate. The reason for this discrepancy is presently unknown, but will likely be illuminated by upcoming experiments.

## V. SUMMARY AND OUTLOOK

In this work, we study OMC on  $^{24}\text{Mg}$  generating transitions to the lowest excited states in  $^{24}\text{Na}$ . We calculate the NMEs based on Morita-Fujii muon-capture formalism and apply the VS-IMSRG ab initio framework to obtain consistent valence-space Hamiltonians and OMC operators. In addition, we use realistic bound-muon wave functions obtained from solving the Dirac equations where the finite size of the nucleus is taken into account. Finally, we calculate the capture rates to the lowest states

in  $^{24}\text{Na}$  with the obtained matrix elements and compare them against existing experimental data.

Comparing the VS-IMSRG results with those of the NSM, we see that explicitly including excitations outside the valence space in the form of the OBTDs generally has strong impact on the NMEs, while the effect coming from consistent transformation of the OMC operators is less significant, with a few exceptions. While we anticipate including IMSRG(3) level corrections to the operators would have a minor influence on the NMEs, such corrections to the effective valence-space Hamiltonian could be important. The VS-IMSRG-computed capture rates are generally smaller than the rates computed in NSM, but the rates to the first and second  $1^+$  states seem to be interchanged, which is partly explained by the mixing of these two states. Comparing with experimental data, we notice that the obtained capture rates are generally smaller than the experimental rates; while the agreement is reasonable for the total transition rate to the  $1^+$  states, both the NSM and VS-IMSRG underestimate the total rate to the  $2^+$  states. The discrepancy could be partly explained by uncertainties in the experimental data, but future measurements will help shed light on this.

The present work serves as the first step towards a systematic ab initio treatment of OMC on nuclei. While the results, compared with NSM results and available data, look promising, it remains as a future task to study further theoretical improvements such as including the small component of the bound-muon wave function, two-body hadronic currents and some approximate IMSRG(3)-level corrections. We are currently extending these studies to all nuclei relevant for upcoming experiments, with the ultimate goal to compare the obtained partial capture rates with experimental data to shed light on effective values of the couplings  $g_A$  and  $g_P$  at momentum-exchange  $q \sim 100$  MeV. This momentum regime is highly relevant for  $0\nu\beta\beta$  decay and thus OMC calculations may help constrain uncertainties related to emerging ab initio predictions of  $0\nu\beta\beta$  decay [64–66].

## ACKNOWLEDGMENTS

We thank J. Menéndez for helpful discussions. This work was supported by the Finnish Cultural Foundation grant No. 00210067, NSERC under grants SAPIN-2018-00027 and RGPAS-2018-522453, the Arthur B. McDonald Canadian Astroparticle Physics Research Institute, the US Department of Energy (DOE) under contract DE-FG02-97ER41014, and Academy of Finland (Grant Nos. 314733, 320062 and 318043). TRIUMF receives funding via a contribution through the National Research Council of Canada. Computations were performed with an allocation of computing resources on Cedar at WestGrid and Compute Canada, and on the Oak Cluster at TRIUMF managed by the University of British Columbia department of Advanced Research Computing (ARC).



- [1] M. Kortelainen and J. Suhonen, Nuclear muon capture as a powerful probe of double-beta decays in light nuclei, *J. Phys. G: Nucl. Part. Phys.* **30**, 2003 (2004).
- [2] M. Kortelainen and J. Suhonen, Ordinary muon capture as a probe of virtual transitions of decay, *Europhys. Lett.* **58**, 666 (2002).
- [3] I. S. Towner, Quenching of spin matrix elements in nuclei, *Phys. Rep.* **155**, 263 (1987).
- [4] P. Gysbers, G. Hagen, J. D. Holt, G. R. Jansen, T. D. Morris, P. Navrátil, T. Papenbrock, S. Quaglioni, A. Schwenk, S. R. Stroberg, and K. A. Wendt, Discrepancy between experimental and theoretical  $\beta$ -decay rates resolved from first principles, *Nature Phys.* **15**, 428–431 (2019).
- [5] V. A. Andreev, T. I. Banks, R. M. Carey, T. A. Case, S. M. Clayton, K. M. Crowe, J. Deutsch, J. Egger, S. J. Freedman, V. A. Ganzha, *et al.*, Measurement of muon capture on the proton to 1% precision and determination of the pseudoscalar coupling  $g_p$ , *Phys. Rev. Lett.* **110**, 012504 (2013).
- [6] T. Siiskonen, J. Suhonen, and M. Hjorth-Jensen, Towards the solution of the  $C_P/C_A$  anomaly in shell-model calculations of muon capture, *Phys. Rev. C* **59**, R1839 (1999).
- [7] M. Kortelainen, M. Aunola, T. Siiskonen, and J. Suhonen, Mean-field effects on muon-capture observables, *J. Phys. G: Nucl. Part. Phys.* **26**, L33 (2000).
- [8] T. Siiskonen, M. Hjorth-Jensen, and J. Suhonen, Renormalization of the weak hadronic current in the nuclear medium, *Phys. Rev. C* **63**, 055501 (2001).
- [9] H. Fearing, R. Lewis, N. Mobed, and S. Scherer, Muon capture by a proton in heavy baryon chiral perturbation theory, *Phys. Rev. D* **56**, 1783 (1997).
- [10] S. Ando and D.-P. Min, Radiative muon capture in heavy baryon chiral perturbation theory, *Phys. Lett. B* **417**, 177 (1998).
- [11] T. Meissner, F. Myhrer, and K. Kubodera, Radiative muon capture by a proton in chiral perturbation theory, *Phys. Lett. B* **416**, 36 (1998).
- [12] D. F. Measday, The nuclear physics of muon capture, *Phys. Rep.* **354**, 243 (2001).
- [13] T. Siiskonen, J. Suhonen, V. A. Kuz'min, and T. V. Tetereva, Shell-model study of partial muon-capture rates in light nuclei, *Nucl. Phys. A* **635**, 446 (1998).
- [14] T. Suzuki, S. Chiba, T. Yoshida, K. Takahashi, and H. Umeda, Neutrino-nucleus reactions on  $^{16}\text{O}$  based on new shell-model hamiltonians, *Phys. Rev. C* **98**, 034613 (2018).
- [15] P. G. Giannaka and T. S. Kosmas, Detailed description of exclusive muon capture rates using realistic two-body forces, *Phys. Rev. C* **92**, 014606 (2015).
- [16] L. Jokiniemi and J. Suhonen, Muon-capture strength functions in intermediate nuclei of  $0\nu\beta\beta$  decays, *Phys. Rev. C* **100**, 014619 (2019).
- [17] F. Šimkovic, R. Dvornický, and P. Vogel, Muon capture rates: Evaluation within the quasiparticle random phase approximation, *Phys. Rev. C* **102**, 034301 (2020).
- [18] M. Ciccarelli, F. Minato, and T. Naito, Theoretical study of nb isotope productions by muon capture reaction on  $^{100}\text{Mo}$ , *Phys. Rev. C* **102**, 034306 (2020).
- [19] A. Lovato, N. Rocco, and R. Schiavilla, Muon capture in nuclei: An *ab initio* approach based on Green's function Monte Carlo methods, *Phys. Rev. C* **100**, 035502 (2019).
- [20] G. B. King, S. Pastore, M. Piarulli, and R. Schiavilla, Partial muon capture rates in  $A = 3$  and  $A = 6$  nuclei with chiral effective field theory (2021), [arXiv:2111.11360 \[nucl-th\]](https://arxiv.org/abs/2111.11360).
- [21] L. Jokiniemi, J. Suhonen, H. Ejiri, and I. H. Hashim, Pinning down the strength function for ordinary muon capture on  $^{100}\text{Mo}$ , *Phys. Lett. B* **794**, 143 (2019).
- [22] I. H. Hashim, H. Ejiri, T. Shima, K. Takahisa, A. Sato, Y. Kuno, K. Ninomiya, N. Kawamura, and Y. Miyake, Muon capture reaction on  $^{100}\text{Mo}$  to study the nuclear response for double- $\beta$  decay and neutrinos of astrophysics origin, *Phys. Rev. C* **97**, 014617 (2018).
- [23] D. Zinatulina, V. Brudanin, V. Egorov, C. Petitjean, M. Shirchenko, J. Suhonen, and I. Yutlandov, Ordinary muon capture studies for the matrix elements in  $\beta\beta$  decay, *Phys. Rev. C* **99**, 024327 (2019).
- [24] S. R. Stroberg, H. Hergert, J. D. Holt, S. K. Bogner, and A. Schwenk, Ground and excited states of doubly open-shell nuclei from *ab initio* valence-space Hamiltonians, *Phys. Rev. C* **93**, 051301 (2016).
- [25] S. J. Novario, G. Hagen, G. R. Jansen, and T. Papenbrock, Charge radii of exotic neon and magnesium isotopes, *Phys. Rev. C* **102**, 051303 (2020).
- [26] T. Suzuki, D. F. Measday, and J. P. Roalsvig, Total nuclear capture rates for negative muons, *Phys. Rev. C* **35**, 2212 (1987).
- [27] T. P. Gorringe, D. S. Armstrong, S. Arole, M. Boleman, E. Gete, V. Kuzmin, B. A. Moftah, R. Sedlar, T. J. Stocki, and T. Tetereva, Measurement of partial muon capture rates in  $1s - 0d$  shell nuclei, *Phys. Rev. C* **60**, 055501 (1999).
- [28] V. V. Belov, V. B. Brudanin, K. N. Gusev, V. G. Egorov, I. V. Zhitnikov, D. R. Zinatulina, S. V. Kazartsev, N. S. Rumyantseva, E. A. Shevchik, M. V. Shirchenko, Y. A. Shitov, and M. V. Fomina, Construction of the Gaseous and Solid-State Targets for the Muon Capture Measuring System in  $^{130}\text{Xe}$ ,  $^{82}\text{Kr}$ , and  $^{24}\text{Mg}$ , *Phys. Part. Nuclei Lett.* **17**, 848–855 (2020).
- [29] H. Hergert, S. K. Bogner, T. D. Morris, A. Schwenk, and K. Tsukiyama, The In-Medium Similarity Renormalization Group: A Novel *Ab Initio* Method for Nuclei, *Phys. Rept.* **621**, 165 (2016).
- [30] S. R. Stroberg, A. Calci, H. Hergert, J. D. Holt, S. K. Bogner, R. Roth, and A. Schwenk, Nucleus-Dependent Valence-Space Approach to Nuclear Structure, *Phys. Rev. Lett.* **118**, 032502 (2017).
- [31] S. R. Stroberg, H. Hergert, S. K. Bogner, and J. D. Holt, Nonempirical Interactions for the Nuclear Shell Model: An Update, *Annu. Rev. Nucl. Part. Sci.* **69**, 307 (2019).
- [32] M. Morita and A. Fujii, Theory of Allowed and Forbidden Transitions in Muon Capture Reactions, *Phys. Rev.* **118**, 606 (1960).
- [33] H. A. Bethe and E. E. Salpeter, *Quantum Mechanics of One- and Two-Electron Atoms* (Academic Press Inc., New York, 1959).
- [34] L. Jokiniemi, J. Kotila, and J. Suhonen, Comparative Analysis of Nuclear Matrix Elements of  $0\nu\beta^+\beta^+$  Decay and Muon Capture in  $^{106}\text{Cd}$ , *Front. Phys.* **9**, 142 (2021).
- [35] F. Salvat, J. Fernández-Varea, and W. Williamson Jr.,

- Accurate numerical solution of the radial Schrödinger and Dirac wave equations, *Comput. Phys. Commun.* **90**, 151 (1995).
- [36] J. Kotila and F. Iachello, Phase-space factors for double- $\beta$  decay, *Phys. Rev. C* **85**, 034316 (2012).
- [37] J. Kotila and F. Iachello, Phase space factors for  $0\nu\beta^+\beta^+$  decay and competing modes of double- $\beta$  decay, *Phys. Rev. C* **87**, 024313 (2013).
- [38] L. Jokiniemi, *Probing neutrinoless double-beta decay by charge-exchange reactions and muon capture*, Ph.D. thesis, University of Jyväskylä, JYU Dissertations 288 (2020), URN:ISBN:978-951-39-8304-8.
- [39] J. Menéndez, D. Gazit, and A. Schwenk, Chiral Two-Body Currents in Nuclei: Gamow-Teller Transitions and Neutrinoless Double-Beta Decay, *Phys. Rev. Lett.* **107**, 062501 (2011).
- [40] M. Hoferichter, P. Klos, and A. Schwenk, Chiral power counting of one- and two-body currents in direct detection of dark matter, *Phys. Lett. B* **746**, 410 (2015).
- [41] S. Pastore, L. Girlanda, R. Schiavilla, M. Viviani, and R. B. Wiringa, Electromagnetic currents and magnetic moments in chiral effective field theory ( $\chi$ EFT), *Phys. Rev. C* **80**, 034004 (2009).
- [42] A. Baroni, L. Girlanda, S. Pastore, R. Schiavilla, and M. Viviani, Nuclear axial currents in chiral effective field theory, *Phys. Rev. C* **93**, 015501 (2016); Errata:, *Phys. Rev. C* **93**, 049902 (2016); *Phys. Rev. C* **95**, 059901 (2017).
- [43] H. Krebs, E. Epelbaum, and U.-G. Meißner, Nuclear axial current operators to fourth order in chiral effective field theory, *Ann. Phys.* **378**, 317 (2017).
- [44] H. Krebs, E. Epelbaum, and U.-G. Meißner, Nuclear electromagnetic currents to fourth order in chiral effective field theory, *Few-Body Syst.* **60**, 31 (2019).
- [45] K. Tsukiyama, S. K. Bogner, and A. Schwenk, In-medium similarity renormalization group for open-shell nuclei, *Phys. Rev. C* **85**, 061304 (2012).
- [46] S. K. Bogner, H. Hergert, J. D. Holt, A. Schwenk, S. Binder, A. Calci, J. Langhammer, and R. Roth, Nonperturbative Shell-Model Interactions from the In-Medium Similarity Renormalization Group, *Phys. Rev. Lett.* **113**, 142501 (2014).
- [47] T. Miyagi, S. R. Stroberg, J. D. Holt, and N. Shimizu, Ab initio multishell valence-space Hamiltonians and the island of inversion, *Phys. Rev. C* **102**, 034320 (2020).
- [48] T. D. Morris, N. M. Parzuchowski, and S. K. Bogner, Magnus expansion and in-medium similarity renormalization group, *Phys. Rev. C* **92**, 034331 (2015).
- [49] N. M. Parzuchowski, S. R. Stroberg, P. Navrátil, H. Hergert, and S. K. Bogner, Ab initio electromagnetic observables with the in-medium similarity renormalization group, *Phys. Rev. C* **96**, 034324 (2017).
- [50] E. Epelbaum, H.-W. Hammer, and U.-G. Meißner, Modern Theory of Nuclear Forces, *Rev. Mod. Phys.* **81**, 1773 (2009).
- [51] R. Machleidt and D. R. Entem, Chiral effective field theory and nuclear forces, *Phys. Rep.* **503**, 1 (2011).
- [52] K. Hebeler, S. K. Bogner, R. J. Furnstahl, A. Nogga, and A. Schwenk, Improved nuclear matter calculations from chiral low-momentum interactions, *Phys. Rev. C* **83**, 031301 (2011).
- [53] J. Simonis, S. R. Stroberg, K. Hebeler, J. D. Holt, and A. Schwenk, Saturation with chiral interactions and consequences for finite nuclei, *Phys. Rev. C* **96**, 014303 (2017).
- [54] T. D. Morris, J. Simonis, S. R. Stroberg, C. Stumpf, G. Hagen, J. D. Holt, G. R. Jansen, T. Papenbrock, R. Roth, and A. Schwenk, Structure of the lightest tin isotopes, *Phys. Rev. Lett.* **120**, 152503 (2018).
- [55] S. R. Stroberg, J. D. Holt, A. Schwenk, and J. Simonis, Ab Initio Limits of Atomic Nuclei, *Phys. Rev. Lett.* **126**, 022501 (2021).
- [56] T. Miyagi, S. R. Stroberg, P. Navrátil, K. Hebeler, and J. D. Holt, Converged ab initio calculations of heavy nuclei (2021), [arXiv:2104.04688 \[nucl-th\]](https://arxiv.org/abs/2104.04688).
- [57] R. de Groote *et al.*, Measurement and microscopic description of odd-even staggering of charge radii of exotic copper isotopes, *Nature Phys.* **16**, 620 (2020).
- [58] M. Heinz, A. Tichai, J. Hoppe, K. Hebeler, and A. Schwenk, In-medium similarity renormalization group with three-body operators, *Phys. Rev. C* **103**, 044318 (2021).
- [59] S. R. Stroberg, <https://github.com/ragnarstroberg/imsrg>.
- [60] N. Shimizu, T. Mizusaki, Y. Utsuno, and Y. Tsunoda, Thick-restart block Lanczos method for large-scale shell-model calculations, *Comput. Phys. Commun.* **244**, 372 (2019).
- [61] B. A. Brown and W. D. M. Rae, The Shell-Model Code NuShellX@MSU, *Nucl. Data Sheets* **120**, 115 (2014).
- [62] B. A. Brown and W. A. Richter, New “USD” Hamiltonians for the  $sd$  shell, *Phys. Rev. C* **74**, 034315 (2006).
- [63] J. Blomqvist and A. Molinari, Collective  $0^-$  vibrations in even spherical nuclei with tensor forces, *Nucl. Phys. A* **106**, 545 (1968).
- [64] J. M. Yao, B. Bally, J. Engel, R. Wirth, T. R. Rodríguez, and H. Hergert, Ab initio treatment of collective correlations and the neutrinoless double beta decay of  $^{48}\text{Ca}$ , *Phys. Rev. Lett.* **124**, 232501 (2020).
- [65] A. Belley, C. G. Payne, S. R. Stroberg, T. Miyagi, and J. D. Holt, Ab Initio Neutrinoless Double-Beta Decay Matrix Elements for  $^{48}\text{Ca}$ ,  $^{76}\text{Ge}$ , and  $^{82}\text{Se}$ , *Phys. Rev. Lett.* **126**, 042502 (2021).
- [66] S. Novario, P. Gysbers, J. Engel, G. Hagen, G. R. Jansen, T. D. Morris, P. Navrátil, T. Papenbrock, and S. Quaglioni, Coupled-Cluster Calculations of Neutrinoless Double- $\beta$  Decay in  $^{48}\text{Ca}$ , *Phys. Rev. Lett.* **126**, 182502 (2021).

## Appendix A

Fig. 3 shows the one- and two-body parts of the VS-IMSRG NMEs compared with the USDB NMEs (which do not contain a two-body part). To evaluate the relative importance of the different (NSM/Vs-IMSRG) nuclear wave functions and operators (HO/Vs-IMSRG-evolved), we show the NMEs obtained with different (OBTD, operator)-combinations in Tables V-X. The HO operators are obtained with  $\hbar\omega=16$  MeV, the same value that was used in the VS-IMSRG evolution. Hence, the (USDB,HO)-combinations do not exactly correspond to the ‘USDB’ NMEs shown in Fig. 2 and 3, where the Blomqvist-Molinari formula was used. The (IMSRG,IMSRG)-combinations in the tables correspond to the VS-IMSRG(1b) NMEs shown in Fig. 3.

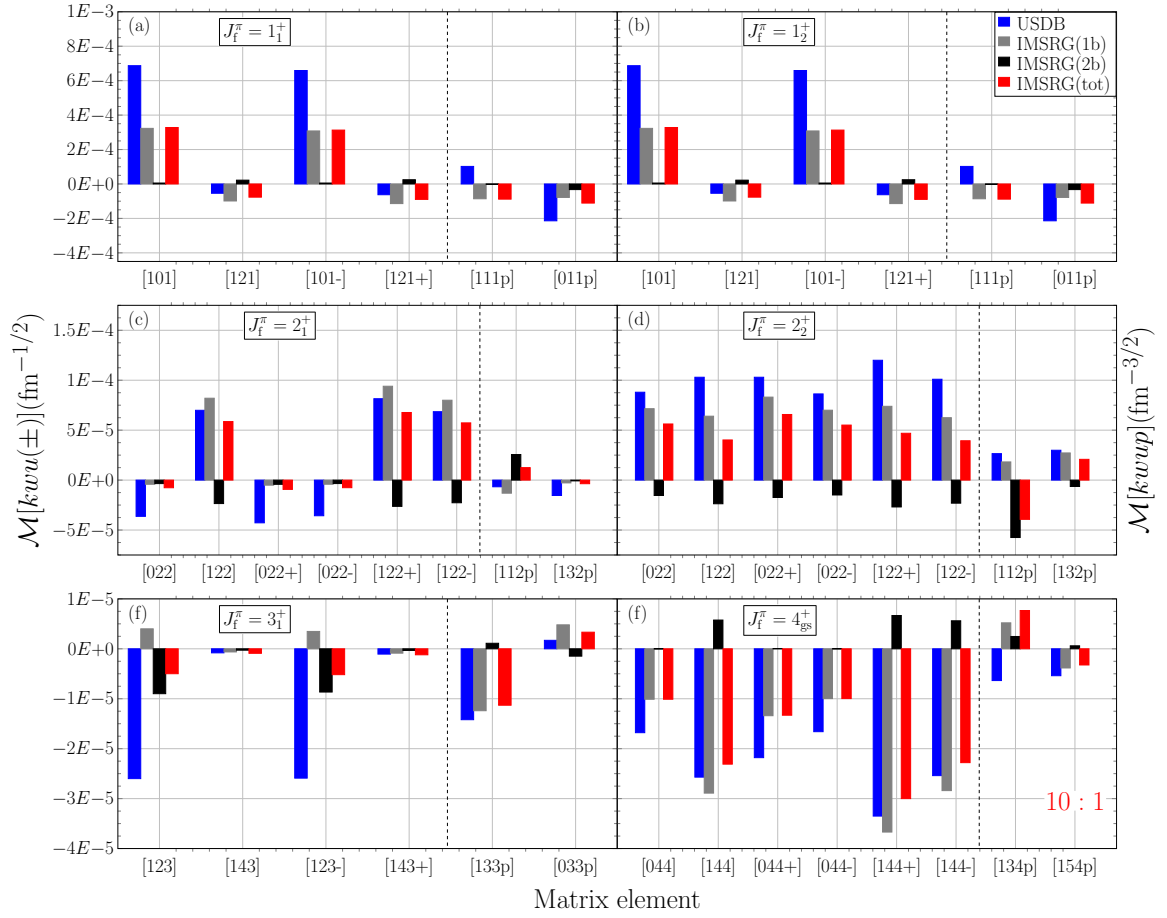


FIG. 3. One-body (gray bars) and two-body (black bars) components of the total VS-IMSRG NMEs (red bars) for  $\mu^- + {}^{24}\text{Mg}(0_{\text{g.s.}}^+) \rightarrow \nu_\mu + {}^{24}\text{Na}(J_i^\pi)$  compared with USDB NMEs (blue bars). NMEs are computed with the exact bound-muon wave function with finite-size nucleus. The NMEs in panel (f) are multiplied by 10.

TABLE V. The NMEs for the transition  $\mu^- + {}^{24}\text{Mg}(0_{\text{g.s.}}^+) \rightarrow \nu_\mu + {}^{24}\text{Na}(1_1^+)$  obtained with different (OBTD, operator)-combinations.

OBTD	operator	[101]	[121]	[101-]	[121+]	[111p]	[011p]
USDB	HO	2.78E-04	5.63E-05	2.69E-04	6.66E-05	3.38E-04	-1.76E-04
USDB	IMSRG	2.96E-04	5.65E-05	2.87E-04	6.63E-05	2.84E-04	-1.63E-04
IMSRG	HO	6.85E-04	3.99E-06	6.64E-04	4.99E-06	2.57E-04	-3.41E-04
IMSRG	IMSRG	5.84E-04	-8.10E-06	5.61E-04	-8.16E-06	2.20E-04	-2.88E-04

TABLE VI. The same as in Table V but for transition  $\mu^- + {}^{24}\text{Mg}(0_{\text{g.s.}}^+) \rightarrow \nu_\mu + {}^{24}\text{Na}(1_2^+)$ .

OBTD	operator	[101]	[121]	[101-]	[121+]	[111p]	[011p]
USDB	HO	7.76E-04	-4.62E-05	7.50E-04	-5.42E-05	1.09E-04	-2.33E-04
USDB	IMSRG	6.33E-04	-7.12E-05	6.07E-04	-8.13E-05	1.00E-04	-1.74E-04
IMSRG	HO	4.44E-04	-7.69E-05	4.29E-04	-9.08E-05	-1.09E-04	-1.25E-04
IMSRG	IMSRG	3.23E-04	-9.88E-05	3.08E-04	-1.14E-04	-8.60E-05	-7.81E-05

TABLE VII. The same as in Table V but for transition  $\mu^- + {}^{24}\text{Mg}(0_{\text{g.s.}}^+) \rightarrow \nu_\mu + {}^{24}\text{Na}(2_1^+)$ .

OBTD	operator	[022]	[122]	[022+]	[022-]	[122+]	[122-]	[112p]	[132p]
USDB	HO	-3.03E-05	5.92E-05	-3.61E-05	-2.99E-05	6.99E-05	5.83E-05	-5.68E-06	-1.29E-05
USDB	IMSRG	-2.77E-05	6.64E-05	-3.25E-05	-2.72E-05	7.62E-05	6.48E-05	-1.88E-05	-1.14E-05
IMSRG	HO	-4.73E-06	7.08E-05	-5.93E-06	-4.74E-06	8.33E-05	6.96E-05	1.63E-06	-3.79E-06
IMSRG	IMSRG	-4.16E-06	8.20E-05	-5.07E-06	-4.13E-06	9.40E-05	8.00E-05	-1.31E-05	-2.81E-06

TABLE VIII. The same as in Table V but for transition  $\mu^- + {}^{24}\text{Mg}(0_{\text{g.s.}}^+) \rightarrow \nu_\mu + {}^{24}\text{Na}(2_2^+)$ .

OBTD	operator	[022]	[122]	[022+]	[022-]	[122+]	[122-]	[112p]	[132p]
USDB	HO	7.44E-05	8.75E-05	8.80E-05	7.32E-05	1.03E-04	8.61E-05	2.27E-05	2.53E-05
USDB	IMSRG	6.74E-05	9.68E-05	7.87E-05	6.60E-05	1.12E-04	9.45E-05	1.15E-05	2.42E-05
IMSRG	HO	7.40E-05	6.08E-05	8.76E-05	7.28E-05	7.18E-05	5.98E-05	1.98E-05	2.70E-05
IMSRG	IMSRG	7.15E-05	6.40E-05	8.31E-05	7.00E-05	7.39E-05	6.25E-05	1.82E-05	2.72E-05

TABLE IX. The same as in Table V but for transition  $\mu^- + {}^{24}\text{Mg}(0_{\text{g.s.}}^+) \rightarrow \nu_\mu + {}^{24}\text{Na}(3_1^+)$ .

OBTD	operator	[123]	[143]	[123-]	[143+]	[133p]	[033p]
USDB	HO	-2.06E-05	-5.33E-07	-2.05E-05	-7.10E-07	-1.18E-05	1.30E-06
USDB	IMSRG	-4.14E-06	-5.25E-07	-4.64E-06	-7.48E-07	-1.24E-05	-1.60E-07
IMSRG	HO	-6.71E-06	-6.75E-07	-6.77E-06	-9.00E-07	-1.16E-05	4.27E-06
IMSRG	IMSRG	4.00E-06	-6.28E-07	3.48E-06	-8.70E-07	-1.24E-05	4.80E-06

TABLE X. The same as in Table V but for transition  $\mu^- + {}^{24}\text{Mg}(0_{\text{g.s.}}^+) \rightarrow \nu_\mu + {}^{24}\text{Na}(4_{\text{g.s.}}^+)$ .

OBTD	operator	[044]	[144]	[044+]	[044-]	[144+]	[144-]	[134p]	[154p]
USDB	HO	-1.11E-06	-1.70E-06	-1.47E-06	-1.10E-06	-2.25E-06	-1.68E-06	-4.27E-07	-3.57E-07
USDB	IMSRG	-7.93E-07	-2.80E-06	-1.06E-06	-7.85E-07	-3.57E-06	-2.76E-06	5.89E-07	-3.15E-07
IMSRG	HO	-1.24E-06	-1.75E-06	-1.64E-06	-1.22E-06	-2.31E-06	-1.73E-06	-4.76E-07	-3.97E-07
IMSRG	IMSRG	-1.01E-06	-2.89E-06	-1.34E-06	-9.97E-07	-3.67E-06	-2.84E-06	5.20E-07	-3.84E-07